Two distinct trimeric conformations of natively membrane-anchored full-length herpes simplex virus 1 glycoprotein B

Tzviya Zeev-Ben-Mordehai[a], Daven Vasishtan[a], Anna Hernández Durán[a,b], Benjamin Vollmer[a], Paul White[a], Arun Prasad Pandurangan[b], C. Alistair Siebert[a], Maya Topf[b], and Kay Grünewald[a,1]

[a]Oxford Particle Imaging Centre, Division of Structural Biology, Wellcome Trust Centre for Human Genetics, University of Oxford, Oxford OX3 7BN, United Kingdom; and [b]Institute of Structural and Molecular Biology, Department of Biological Sciences, Birkbeck College, University of London, London WC1E 7HX, United Kingdom

Edited by Robert A. Lamb, Howard Hughes Medical Institute and Northwestern University, Evanston, IL, and approved February 26, 2016 (received for review November 23, 2015)

Many viruses are enveloped by a lipid bilayer acquired during assembly, which is typically studded with one or two types of glycoproteins. These viral surface proteins act as the primary interface between the virus and the host. Entry of enveloped viruses relies on specialized fusogen proteins to help merge the virus membrane with the host membrane. In the multicomponent herpesvirus fusion machinery, glycoprotein B (gB) acts as this fusogen. Although the structure of the gB ectodomain postfusion conformation has been determined, any other conformations (e.g., prefusion, intermediate conformations) have so far remained elusive, thus restricting efforts to develop antiviral treatments and prophylactic vaccines. Here, we have characterized the full-length herpes simplex virus 1 gB in a native membrane by displaying it on cell-derived vesicles and using electron cryotomography. Alongside the known postfusion conformation, a novel one was identified. Its structure, in the context of the membrane, was determined by subvolume averaging and found to be trimeric like the postfusion conformation, but appeared more condensed. Hierarchical constrained density-fitting of domains unexpectedly revealed the fusion loops in this conformation to be apart and pointing away from the anchoring membrane. This vital observation is a substantial step forward in understanding the complex herpesvirus fusion mechanism, and opens up new opportunities for more targeted intervention of herpesvirus entry.

membrane fusion | class III viral fusion protein | prefusion conformation | electron cryotomography | subvolume averaging

Although nonenveloped viruses have developed ways to escape the endosomal degradation pathway by rupturing and penetrating the respective membranes, entry of enveloped viruses relies on specialized fusogen proteins to help merge the virus membrane with the host membrane (1). Viral membrane fusion can occur directly with the plasma membrane or, topologically identically, at a specific point out of the endosomal network (2).

Herpesviruses are enveloped dsDNA viruses with a complex structure (3, 4). The membrane envelope of herpesviruses is atypically diverse, because it is studded with about a dozen different types of viral glycoproteins (5). Compared with other viruses, entry of herpesviruses is a complex process mediated by multiple viral glycoproteins and host receptors (6). For HSV-1, it is well accepted that glycoprotein D (gD), glycoprotein B (gB), glycoprotein H (gH), and glycoprotein L (gL) constitute the fusion machinery, with the latter three being conserved across the entire herpesvirus family. Based on the available crystal structures, it was suggested that gB catalyzes the membrane fusion itself, whereas the heterodimer gH/gL plays a regulatory role (7–11).

Viral fusion proteins usually exist on the viral membrane surface in a metastable state, a prefusion conformation, and undergo remarkable structural rearrangements while promoting membrane merging, resulting in an energetically more stable postfusion conformation (12). Postfusion conformations have been determined by X-ray crystallography for the gB ectodomains from the alphaherpesvirus HSV-1 (10); from the gammaherpesvirus EBV (8); and, most recently, from the betaherpesvirus cytomegalovirus (13, 14). All structures adopt a highly similar "hairpin" conformation, with the two membrane interacting regions [the fusion loops (FLs) and the ectodomain C terminus] located on one end of the protein. The characteristic secondary structure topology, along with the presence of a central trimeric coiled coil, has led to herpesvirus gB being classified as a class III viral membrane fusion protein (15). In all cases, obtaining the crystal structures required the removal of the transmembrane and cytoplasmic domains of gB, likely causing the protein to adopt a postfusion conformation spontaneously, as observed for other fusion proteins (16, 17).

Here, we studied full-length HSV-1 gB on cell-derived vesicles using electron cryotomography (cryoET) to characterize its structure in a native membrane and to get possible access to metastable states. Indeed, two forms were observed on the membrane, revealing, in addition to the known trimeric postfusion form, a new shorter and more condensed conformation. Subsequent subvolume averaging of the latter, followed by hierarchical constrained density-fitting of domains unveiled the FLs in this new and likewise trimeric form to be separated and pointing away from the anchoring membrane. These results, combined with previous knowledge, lead

Significance

Successful host cell infection requires that viruses get various components—most importantly, their genomes—across the bounding membranes into the cytosol. For enveloped viruses, this crucial part of the entry process is achieved by merging the viral membrane with the host membrane, a process mediated by specialized virus-encoded fusion proteins residing on the virus envelope. Accordingly, these surface viral proteins constitute important targets for antiviral treatments as well as for prophylactic vaccine development. Herpesviruses are ubiquitous, opportunistic DNA viruses that have mastered immune system evasion to cause lifelong infections, with intermittent clinical and subclinical viral reactivation. The structural information on an effective glycoprotein B conformation reported here opens up overdue opportunities for targeted interventions in herpesvirus entry.

Author contributions: T.Z. and K.G. designed research; T.Z., D.V., A.H.D., B.V., P.W., and C.A.S. performed research; T.Z., D.V., A.H.D., B.V., A.P.P., M.T., and K.G. analyzed data; and T.Z., D.V., A.H.D., and K.G. wrote the paper.

The authors declare no conflict of interest.

This article is a PNAS Direct Submission.

Data deposition: The final gB reconstruction and the coordinates of the pseudoatomic model have been deposited in the Electron Microscopy Data Bank (EMDB) at the Protein Data Bank in Europe (PDBe), www.ebi.ac.uk/pdbe/emdb/ (accession code EMD-3362 and PDB code 5FZ2).

[1]To whom correspondence should be addressed. Email: kay@strubi.ox.ac.uk.

This article contains supporting information online at www.pnas.org/lookup/suppl/doi:10.1073/pnas.1523234113/-/DCSupplemental.

us to propose a revised model for the conformational changes catalyzing membrane fusion.

Results and Discussion

Characterization of Full-Length HSV-1 gB on Extracellular Vesicles. To study full-length HSV-1 gB in a native membrane, it was displayed on cell-derived membrane vesicles. In these extracellular vesicles, proteins are natively anchored with correct topology in genuine biological membranes (18). Vesicles with full-length HSV-1 gB were collected from the culture medium of adherent mammalian cells at 48 h posttransfection with the gene for HSV-1 gB and then purified by differential centrifugation (details are provided in *Materials and Methods*), resulting in high yields of vesicles. The specific enrichment and the identity of the proteins incorporated were validated by SDS/PAGE, Western blot analysis (Fig. S1 *A*–*C*), MS using an exponentially modified protein abundance index (emPAI; Table S1), and immunogold labeling (Fig. S1 *D* and *E*). Under denaturing and reducing conditions, gB on the vesicles had an apparent molecular mass of ∼120 kDa, and under seminative conditions, it had an apparent molecular mass of ∼250 kDa (Fig. S1), consistent with the molecular mass observed for mature gB extracted from virions and infected cells (19). The emPAI not only verified the SDS/PAGE results that HSV-1 gB was the most abundant protein in the vesicle preparation but also, importantly, detected no other integral membrane proteins (Table S1). Immunogold labeling using a polyclonal anti-gB Ab readily detected the protein on the vesicle membranes (Fig. S1 *D* and *E*).

Two Trimeric Forms of gB Clearly Differing in Shape and Height Are Present on Vesicle Membranes. Electron cryomicroscopy (cryoEM) imaging of the gB-enriched vesicles showed that they were mainly spherical and studded with proteins, which appeared as discrete densities (Fig. 1*A*). At least two kinds of protein densities of different lengths and shapes were observed, being clearly discernible in cryoET slices (Fig. 1 *B* and *C*). Together with the MS results, these findings indicated that, for the first time to our knowledge, a conformation other than the postfusion trimer of gB had become amenable to further characterization.

The mean diameter of the vesicles was related to the predominant protein conformation on its surface (Fig. 1*D*). The majority (>80%) of the vesicles had a normal distribution of sizes, with a mean diameter of ∼110 nm. On those vesicles, the protein densities were roughly globular, with a height of ∼10 nm. A smaller fraction of the vesicles (<5%) had a smaller mean diameter, and the protein densities on the surface had a height of ∼16 nm (Fig. 1 *A* and *B*). On some of the vesicles, both types of densities were found.

Chemical cross-linking was used to determine the oligomeric state of gB on the vesicle membrane. The gB vesicles were incubated with either the membrane-impermeable cross-linker bis[sulfosuccinimidyl] suberate, which has a spacer arm length of 11.4 Å, or the membrane-permeable cross-linkers disuccinimidyl tartrate and 1,5-difluoro-2,4- dinitrobenzene (DFDNB), which have a spacer arm length of 6.4 Å and 3.0 Å, respectively. All three of them cross-link primary amines (and thiol, imidazolyl, and phenolate groups, in the case of DFDNB). A band, corresponding to a gB trimer, was observed for all of the cross-linkers, albeit with different efficiency depending on the cross-linker concentration (Fig. S1*C*).

Three-Dimensional Reconstructions of the Two Forms of gB on the Membrane. To characterize the two conformations of gB at higher resolution, we applied cryoET and averaging of tomographic subvolumes (details are provided in *Materials and Methods*). For both forms, subvolumes were manually picked at the vesicle surfaces. These volumes were then each iteratively aligned and averaged in a reference-free manner with 1,909 (short form) and 395 (long form) subvolumes contributing to the final averages (Figs. S2 and S3). The resulting 3D reconstructions of the short and long forms (Fig. 2) were determined to have a resolution of 23 Å and 31 Å, respectively, at the 0.143 threshold based on the gold-standard criterion (Fig. S4). The lower resolution of the long-form reconstruction is likely a result of a considerably smaller dataset. Although the two reconstructions were markedly different (Fig. 2), both showed clear threefold symmetry with an axis normal to the membrane. This symmetry was already apparent in the early steps of the refinement. During later steps, threefold symmetry was applied (Figs. S2 and S3).

The short and more condensed form had an ectodomain measuring 10 nm in height and 8 nm in width (Fig. 2 *A*–*C*). It was anchored to the membrane by three densities ∼6 nm apart, forming a tripod (Fig. 2*B*), whereas on the inside of the membrane, a central density ∼1.5 nm in height and ∼3 nm in width was observed (Fig. 2*C*). The ectodomain had its maximal lateral extension at a height of 4 nm from the membrane. At this height, neighboring trimers contacted each other, forming a pseudolattice (Fig. S5) with variable neighbor occupancies and relative

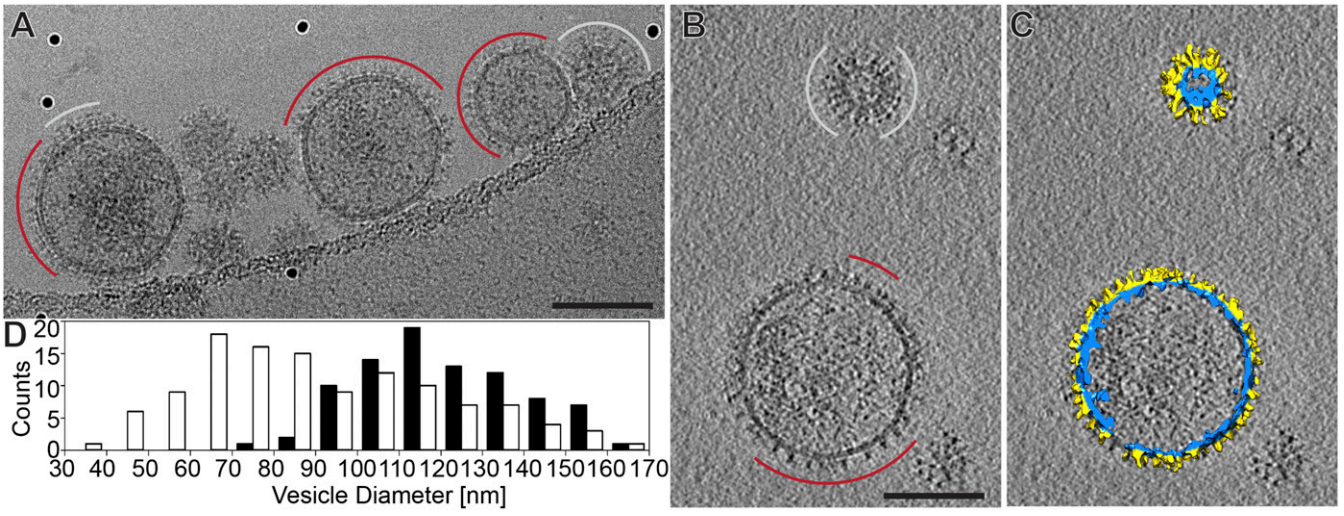

Fig. 1. Full-length HSV-1 gB on cell-derived extracellular vesicles. (*A*) CryoEM projection image. Red arcs indicate the gB short form, and white arcs indicate the gB long form. (*B*) Slice from cryotomogram. Colors as in *A*. (*C*) Three-dimensional rendering of the tomogram shown in *B*. The membrane is colored blue, and the protein is colored yellow. (*D*) Mean diameter of vesicles displaying predominantly the short form (solid bars) and long (white bars) forms. (Scale bars, 100 nm.)

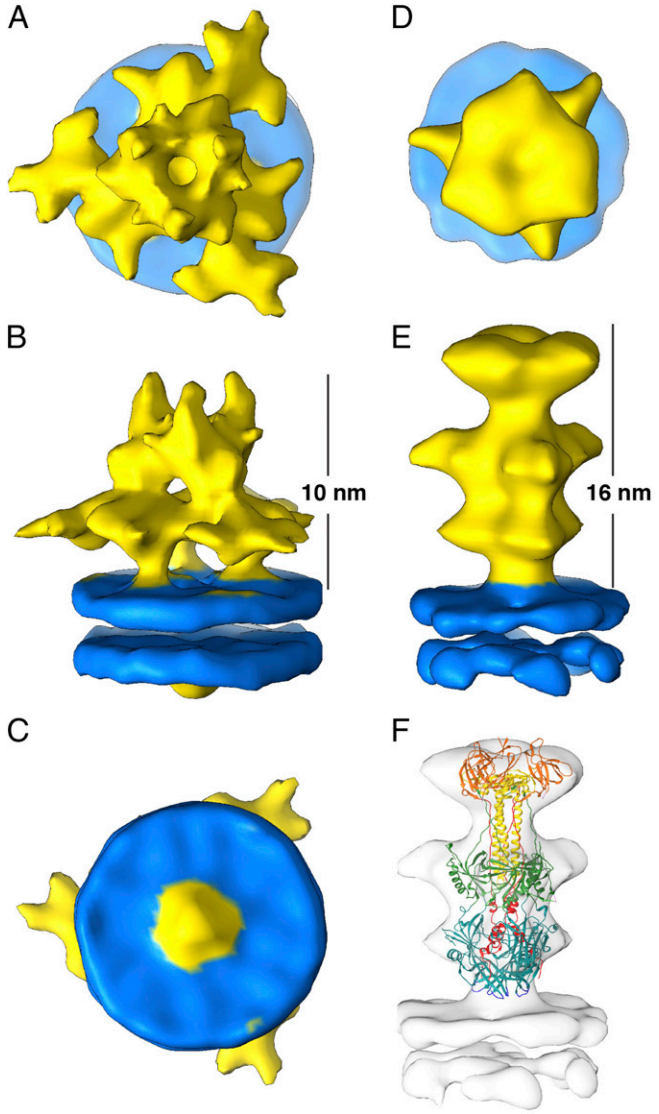

Fig. 2. Subvolume averaging of the two conformations of gB on the vesicle surface. (*A*–*C*) Isosurface representation of the gB short-form 3D reconstruction. Three orthogonal views are presented. The membrane is colored blue, and the protein is colored yellow. (*D* and *E*) Isosurface representation of the gB long-form 3D reconstruction. Two orthogonal views are presented; colors are as in *A*. (*F*) Three-dimensional reconstruction of the long form (as in *E*, colored white) with the postfusion crystal structure fitted [Protein Data Bank (PDB) ID code 2GUM]. Domains are colored as in the original publication (10).

position inconsistencies. Most distal to the membrane were three oblong densities, with their tips pointing away from the membrane in an angle to the bilayer and creating a central cavity between them (Fig. 2 *A* and *B*).

The long-form ectodomain was ∼16 nm in height and was anchored to the membrane through a single central density (Fig. 2 *D* and *E*). This form was highly similar in shape to the postfusion crystal structure of gB (8, 10, 13, 14) and the 3D reconstruction of the ectodomain bound to liposomes (20). This conformation appeared predominantly on the smaller vesicles, indicating that the postfusion form of gB prefers higher curvature, as observed previously on HSV-1 virions (20). The trimeric postfusion crystal structure could be fitted as one rigid body in the EM map (Fig. 2*F*).

Model of gB Short Conformation. To derive the model of the short-form ectodomain, we applied a hierarchical rigid domain-fitting approach based on large ensembles generated by four independent fitting methods. The postfusion crystal structure of HSV-1 gB defined five domains (8, 10, 13, 14). Domain I is the largest and most distinct in shape, containing the FLs that are vital for inducing membrane merging. It is connected to the globular domain II by two short linkers. To position domain I in the map, we generated independent ensembles using four different global search rigid domain-fitting methods (Fig. S6). Ranking, clustering, and filtering of these ensembles resulted in two groups of possible orientations for domain I, both at the membrane distal part of the EM map but oriented roughly 180° relative to each other (Fig. S6). Applying domain II distance constraints allowed us to discard one group of solutions, leaving only those solutions with the FLs pointing away from the membrane (Fig. 3 and Movie S1).

The positioning of domain I most distal to the membrane and the FLs pointing away was unexpected, representing a fundamentally different arrangement from the arrangement found in the membrane-bound postfusion trimer (20) (Fig. 2*F*) that presents the molecule in a conformation more prone for interaction with a target membrane.

The most distinct difference between the condensed form of gB and the postfusion one is the FLs between protomers being ∼5 nm apart. Notably, the orientation of domains I and II relative to the threefold symmetry axis between the two conformations is different, thus leading to a different surface of domains I and II being exposed (Fig. 4 and Movie S2). Moreover, glycosylation site N398 is on the surface and directly facing neighboring gB trimers, suggesting that it might be involved in interprotein interactions (Fig. 4 and Fig. S5).

Studies of Abs that neutralize HSV-1 infection have identified several antigenic sites on gB (21, 22). A major antigenic site on gB is on domain II, as is the case for the rhabdovirus glycoprotein (23). This domain presents an extensive exposed surface in the condensed conformation model, with epitopes for the neutralizing Abs H1781 (residues 454–473) and H1838 (residues 390–410) being exposed. Of particular interest is a recently raised anti-FL2 polyclonal Ab (residues 258–260). Reported data for this Ab indicated that the FLs are accessible on the virus (22). Although this observation could not be reconciled with the previously available postfusion structure of gB, these data are consistent with the condensed conformation on the membrane with the FL exposed presented here. Taken together, all of the available data on neutralizing Abs mapped to domains I and II, which could not be explained previously on the basis of the gB postfusion structure alone, are consistent with the new conformation of gB described here and support its assignment as a prefusion conformation or an intermediate.

Extensive mutational analyses of HSV-1 gB have been previously reported. Specifically, random linker-insertion mutagenesis (24) and fluorescence protein insertion mutagenesis (25) identified positions of the protein that tolerated insertions, thus permitting processing and transport of mutated gB to the plasma membrane and positions that did not tolerate insertions. All of the reported positions tolerating insertions are on the surface of the condensed gB conformation model (Fig. 4*A*). The successful insertion at position A261 of FL2, and its subsequent expression on cell surfaces (24), is consistent with the FLs being accessible in the metastable state of gB before fusion and in agreement with the antigenic data mentioned above. Furthermore, the two residues I185 and E187 in the β-sheet leading to FL1 are surface-exposed in the condensed conformation (Fig. 4*A*), thus permitting the reported expression of insertion mutations in these positions (24). However, these residues are buried in the postfusion conformation (Fig. 4*B*), making these mutants nonfunctional (24) (i.e., prohibiting the conformational change to the latter). Linker insertions can potentially interfere in any level of protein folding and processing (i.e., secondary structure, tertiary structure, quaternary structure). Of the many positions not tolerating insertions, a few are intriguing because they could not be explained by the postfusion structure alone but can now be explained by the swap in exposed surfaces observed between the two conformations (Fig. 4). For example, the insertion at position A334 was expected to be tolerated based on the postfusion structure because it is in a big loop on the surface; however, in the condensed form, this loop is

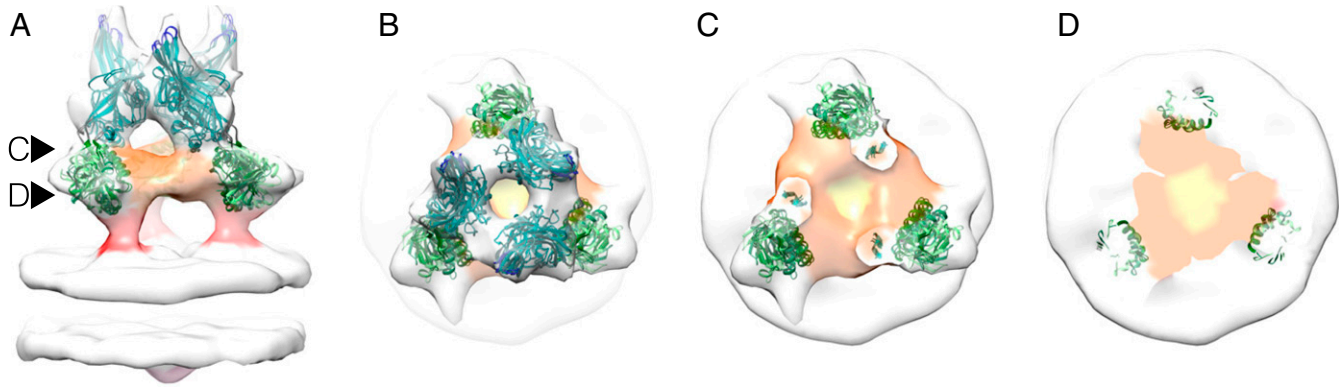

Fig. 3. Modeling of the novel conformation of gB. Isosurface representation of the novel conformation (as in Fig. 2 *A*–*C*) with an ensemble (four models, details are provided in *Materials and Methods*) of domains I (cyan) and II (green) fitted; the FLs are colored blue. The regions of the map corresponding to domain IV (Fig. S7) are colored orange. The regions of the map most likely corresponding to domains III and V (including the membrane proximal region) are colored yellow and red, respectively (also Movie S1). (*A*) Side view. (*B*) Top view. (*C* and *D*) Slices through the 3D reconstruction at the planes marked in *A*.

much more centrally positioned and faces a helix from an adjacent protomer that, likewise, did not tolerate insertions (positions 193–203). Together, these experimental data further validate the condensed conformation as relevant and being significantly different in domain topology from the postfusion form.

The core of the gB postfusion conformation is composed of a trimeric coiled coil (domain III) with the long C-terminal arms (domain V) packed against it in an antiparallel manner, a feature that is typical for class I viral fusion proteins (26). Domain IV is a globular domain located between domains III and V, and it is known to be significantly repositioned between the pre- and postfusion conformations of vesicular stomatitis virus glycoprotein (VSV G) (27). Domain IV also shows high variability between class III fusion proteins and has intrinsic flexibility (15). To

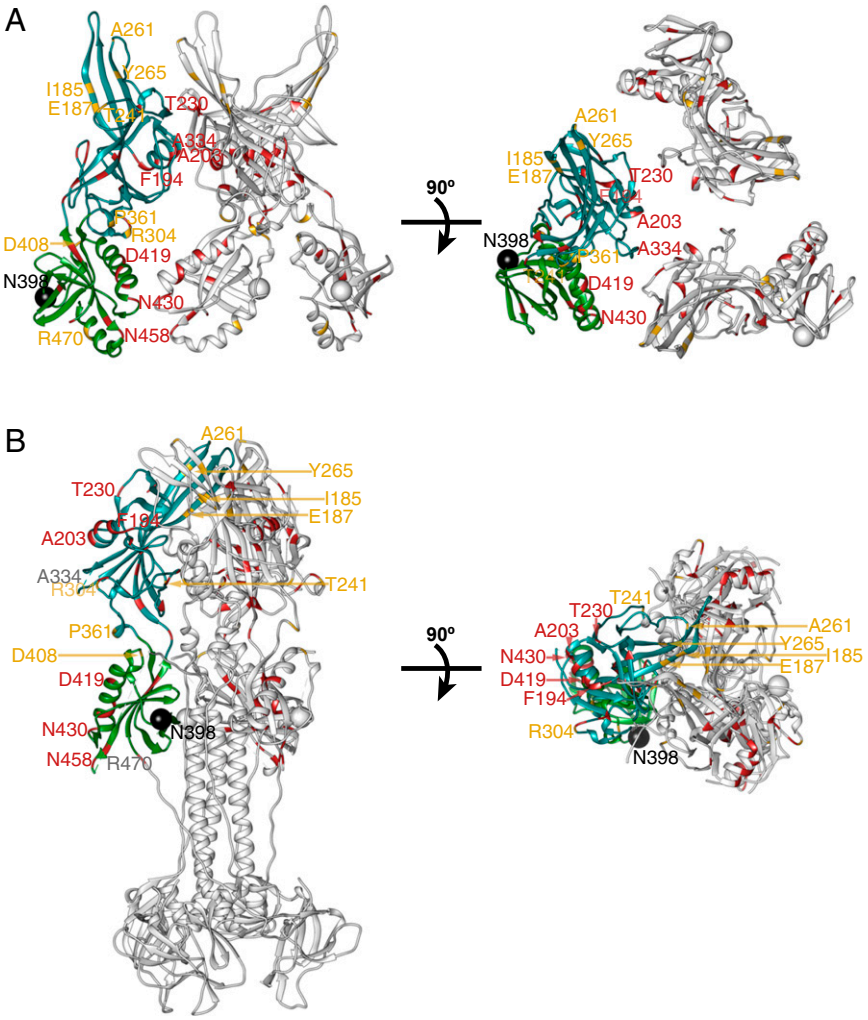

Fig. 4. Comparison between the model of the new conformation and the postfusion conformation of gB with mapping of previously reported insertion mutational analyses. Ribbon representation of two orthogonal views of the new conformation for domains I and II (*A*) and the postfusion conformation (*B*) (PDB ID code 2GUM). Mapped on the structures are reported positions permitting 5-aa insertions (24) or fluorescence protein insertions (25) permitting subsequent plasma membrane expression (colored yellow) and positions not permitting insertions (colored red). Glycosylation site N398 is marked with a black sphere. For each structure, one protomer is colored according to domains, as in Fig. 3, and the other two protomers are colored gray (Movie S2). For each, the left column shows the side view and the right column shows the view from the FL face.

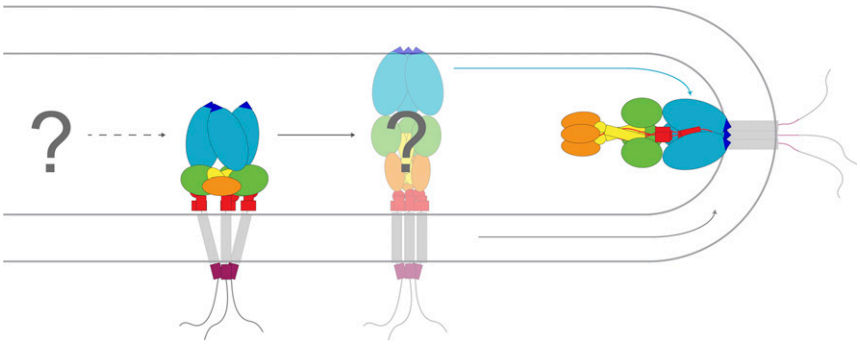

Fig. 5. Proposed model for gB domain rearrangement during fusion. Either at the prefusion state and/or intermediate state, gB is compact, with the FLs apart and pointing away from the viral membrane. After triggering, the protein extends to interact with the target membrane. Extension is likely driven by domain III (yellow), like in VSV G. Domain I (cyan) undergoes rotation, and the FLs (blue triangles) come together to form a hydrophobic patch. Zippering of the long arms of domain V (red) along the trimer leads to the formation of the postfusion hairpin and membrane merging. Domain coloring is as in Fig. 3.

consider the position of this domain in the map, a large ensemble was again generated, scored, clustered, and filtered (Fig. S8). The results of these analyses indicated that domain IV is located in the map's central density area (domain IV, colored orange in Fig. 3) next to domain II and at the same height from the membrane. However, the specific orientation was not fully conclusive (Fig. S8). Domain III could not be confidently fitted in our map. Although the limited resolution is a partial cause, the expected substantial refolding of domain III based on the VSV G pre- and postfusion structures presents a major obstacle for placing them in the map. However, because they are expected to form the trimerization interface, they are most likely to be centrally located in the map, a possibility that our model accommodates (Fig. 3, yellow densities and Movie S1). Finally, because the C terminus of the ectodomain consists of domain V and the as yet structurally uncharacterized highly hydrophobic membrane proximal region, we assigned them to the density forming the tripod (Fig. 3, red densities and Movie S1). Together, domain fitting and further domain assignments based on connectivity and previous information account very well for the overall volume of the short conformation map.

Comparison Between the Two Conformations of HSV-1 gB and the Pre- and Postfusion Conformations of VSV G. HSV-1 gB is the largest and most complex member of the class III viral fusion proteins (15). Unlike VSV G, it is part of a multicomponent fusion machinery and its transition from pre- to postfusion conformation is not assumed to be at least solely pH-dependent or reversible on the viral membrane. Despite the functional and structural differences observed between the postfusion forms of gB and VSV G, a comparison between the condensed conformation of gB and the prefusion form of VSV G (27) highlights some common features (Fig. S9). Both are about two-thirds the height of their postfusion forms but are wider, and the FLs of both are ~5 nm apart.

Proposed Model for gB Domain Rearrangement During Fusion. The two conformational states of gB in the membrane reported here (Figs. 1 and 2), combined with previous knowledge, allow us to propose the following mechanism for how conformational changes in gB promote membrane fusion (Fig. 5). Upon receptor binding to gD, gH/gL triggers a prefusion form of gB to undergo a significant rearrangement. The short conformation reported here, stretching out from the membrane only two-thirds of the height compared with the postfusion form, likely facilitates interaction with the other components of the herpesvirus fusion machinery that share the same approximate height. Assuming that the trimer is preserved throughout the conformational change, the most likely route would be, concomitant to the formation of the coiled-coil core of domain III, a rotation of domain I combined with a petal-like "closing" movement. This movement leads to close proximity of the FLs from all three protomers (from an ~5 nm pairwise distance to direct contact) and results in the formation of a hydrophobic fusion patch. Elevated by the coiled-coil formation of domain III, this fusion patch would contact the target membrane, which is held in a reachable distance by the receptor interaction of gD, and enable insertion into the outer leaflet of the bilayer (20) (Fig. 5), resulting in a gB trimer anchored by the transmembrane region on the viral membrane and with its FLs in the host cell membrane. Formation of the hairpin by zippering of the long arms of domain V along the trimer would conclude the conformational change and complete the membrane merging as suggested for class II viral fusion proteins (28).

Concluding Remarks. Regardless whether the new conformation described here is a prefusion conformation or an intermediate, it is only the second viral class III protein to be reported as not being in a postfusion conformation (27), and, to our knowledge, the first to have been determined in detail fully intact and membrane-anchored. Both this context and resolution allowed the orientation of the protein, and, in particular, the position of the FLs to be deduced. This unexpected and crucial insight represents a significant breakthrough in understanding the class III viral fusion protein mechanism, and provides new opportunities for probing new functional interfaces in the complex herpesvirus fusion machinery and for structure-guided approaches to intervene in herpesvirus entry.

Materials and Methods

Vesicle Preparation. Vesicles enriched with HSV-1 gB in the membrane were produced as recently described, with small modifications in the protocol (18, 29). In brief, baby hamster kidney (BHK-21) cells were transiently transfected with the plasmid for gB [pPEP98 (30)] using Lipofectamine (Invitrogen). Transfected cells were cultured at 37 °C at 5% CO_2 in Glasgow minimum essential medium (GMEM), 20 mM Hepes (pH 7.4), and 2% (vol/vol) tryptose phosphate broth supplemented with 2% (vol/vol) FBS. After 24 h, the culture medium was changed to serum-free medium. Vesicles were collected and purified by differential centrifugation 48 h posttransfection as follows. The medium was collected and cleared from cell debris by centrifugation at 3,000 × *g* for 20 min and at 4 °C; vesicles were then pelleted through a 20% sucrose cushion at 100,000 × *g* and resuspended after careful removal of any supernatant and wall-adherent material in 25 mM Hepes (pH 7.4) and 130 mM NaCl. The vesicle preparations were independently repeated 15 times, each starting from a fresh tissue culture. For every vesicle preparation, at least two aliquots were analyzed by cryoEM.

Chemical Cross-Linking. Cross-linkers (Pierce) were dissolved to a stock concentration in 0.2 M triethanolamine (pH 8.0) or DMSO. For each reaction, 5 μL of gB vesicle sample was mixed with final concentrations of cross-linker at 5 mM, 2.5 mM, 1.25 mM, and 0 mM (control). Reactions were incubated for 30 min at room temperature and were quenched using SDS/PAGE sample buffer. The results were analyzed by SDS/ PAGE and silver-stained.

CryoEM Data Collection and Tomographic Reconstruction. Microscopy was performed at 300 keV using a TF30 "Polara" electron microscope (FEI) equipped with a Quantum postcolumn energy filter (Gatan) operated in zero-loss imaging mode with a 20-eV energy-selecting slit. Images were recorded on a postfilter ~4,000 × 4,000 K2-summit direct electron detector (Gatan) operated in counting mode with dose fractionation, with a calibrated pixel size of 0.23 nm at the specimen level. Tilt series were collected at 300 keV using SerialEM (31) at defocus ranges of −6 to −3 μm. During data collection, the autofocusing routine was iterated to achieve a very stable defocus through the tilt series with 100-nm accuracy. Tomographic reconstructions were calculated in IMOD using weighted back-projection (32). Defocus determination and phase flip according to the contrast transfer function were done in IMOD.

Subvolume Averaging. Particle subvolumes were picked manually and aligned and averaged using PEET 1.9 (33). Gold-standard Fourier shell correlation (FSC) calculation was performed by splitting the dataset into odd and even particles, and applying the same refinement procedure to both independently. The split averages were aligned and masked using a custom mask based on segmentation of the merged average. To avoid correlation between the masks, one average was masked with a hard-edged mask and the other with a soft-edged one. The FSC was calculated using Bsoft (34).

Details are provided in *SI Materials and Methods*. A detailed description of the model building protocol is also found in *SI Materials and Methods*.

ACKNOWLEDGMENTS. We thank C. Whittle for her assistance with sample preparation and I. Farabella for help with density-fitting. We thank Gary H. Cohen and Roselyn J. Eisenberg (University of Pennsylvania) for providing anti-gB Abs. This work was supported by Grant RGY0079/2009-C from the Human Frontiers Science Programme (to K.G. and M.T.), Wellcome Trust Senior Research Fellowship 090895/Z/09/Z (to K.G.), Wellcome Trust Joint Infrastructure Fund Award 060208/Z/00/Z and Wellcome Trust Equipment Grant 093305/Z/10/Z to the Oxford Particle Imaging Centre, Wellcome Trust Core Award 090532/Z/09/Z to the Wellcome Trust Centre for Human Genetics, Leverhulme Trust Grant RPG-2012-519 (to K.G. and M.T.), Biotechnology and Biological Sciences Research Council Tools and Resources Development Fund Grant BB/K01692X/1 (to M.T.), and Marie-Curie Individual Fellowship KGBVIFEF (to B.V.).

1. Martens S, McMahon HT (2008) Mechanisms of membrane fusion: Disparate players and common principles. *Nat Rev Mol Cell Biol* 9(7):543–556.
2. Mercer J, Schelhaas M, Helenius A (2010) Virus entry by endocytosis. *Annu Rev Biochem* 79:803–833.
3. Grünewald K, et al. (2003) Three-dimensional structure of herpes simplex virus from cryo-electron tomography. *Science* 302(5649):1396–1398.
4. Pellett P, Roizman B (2007) The family Herpesviridae: A brief introduction. *Fields Virology*, eds Knipe D, Howley PM (Lippincott, Williams and Wilkins, Philadelphia), 5th Ed, pp 2479–2499.
5. Loret S, Guay G, Lippé R (2008) Comprehensive characterization of extracellular herpes simplex virus type 1 virions. *J Virol* 82(17):8605–8618.
6. Connolly SA, Jackson JO, Jardetzky TS, Longnecker R (2011) Fusing structure and function: A structural view of the herpesvirus entry machinery. *Nat Rev Microbiol* 9(5): 369–381.
7. Backovic M, et al. (2010) Structure of a core fragment of glycoprotein H from pseudorabies virus in complex with antibody. *Proc Natl Acad Sci USA* 107(52):22635–22640.
8. Backovic M, Longnecker R, Jardetzky TS (2009) Structure of a trimeric variant of the Epstein-Barr virus glycoprotein B. *Proc Natl Acad Sci USA* 106(8):2880–2885.
9. Chowdary TK, et al. (2010) Crystal structure of the conserved herpesvirus fusion regulator complex gH-gL. *Nat Struct Mol Biol* 17(7):882–888.
10. Heldwein EE, et al. (2006) Crystal structure of glycoprotein B from herpes simplex virus 1. *Science* 313(5784):217–220.
11. Matsuura H, Kirschner AN, Longnecker R, Jardetzky TS (2010) Crystal structure of the Epstein-Barr virus (EBV) glycoprotein H/glycoprotein L (gH/gL) complex. *Proc Natl Acad Sci USA* 107(52):22641–22646.
12. Harrison SC (2015) Viral membrane fusion. *Virology* 479-480:498–507.
13. Chandramouli S, et al. (2015) Structure of HCMV glycoprotein B in the postfusion conformation bound to a neutralizing human antibody. *Nat Commun* 6:8176.
14. Burke HG, Heldwein EE (2015) Crystal Structure of the Human Cytomegalovirus Glycoprotein B. *PLoS Pathog* 11(10):e1005227.
15. Backovic M, Jardetzky TS (2009) Class III viral membrane fusion proteins. *Curr Opin Struct Biol* 19(2):189–196.
16. Kadlec J, Loureiro S, Abrescia NG, Stuart DI, Jones IM (2008) The postfusion structure of baculovirus gp64 supports a unified view of viral fusion machines. *Nat Struct Mol Biol* 15(10):1024–1030.
17. Yin HS, Paterson RG, Wen X, Lamb RA, Jardetzky TS (2005) Structure of the uncleaved ectodomain of the paramyxovirus (hPIV3) fusion protein. *Proc Natl Acad Sci USA* 102(26):9288–9293.
18. Zeev-Ben-Mordehai T, Vasishtan D, Siebert CA, Whittle C, Grünewald K (2014) Extracellular vesicles: A platform for the structure determination of membrane proteins by Cryo-EM. *Structure* 22(11):1687–1692.
19. Claesson-Welsh L, Spear PG (1986) Oligomerization of herpes simplex virus glycoprotein B. *J Virol* 60(2):803–806.
20. Maurer UE, et al. (2013) The structure of herpesvirus fusion glycoprotein B-bilayer complex reveals the protein-membrane and lateral protein-protein interaction. *Structure* 21(8):1396–1405.
21. Bender FC, et al. (2007) Antigenic and mutational analyses of herpes simplex virus glycoprotein B reveal four functional regions. *J Virol* 81(8):3827–3841.
22. Cairns TM, et al. (2014) Mechanism of neutralization of herpes simplex virus by antibodies directed at the fusion domain of glycoprotein B. *J Virol* 88(5):2677–2689.
23. Baquero E, et al. (2015) Structure of the low pH conformation of Chandipura virus G reveals important features in the evolution of the vesiculovirus glycoprotein. *PLoS Pathog* 11(3):e1004756.
24. Lin E, Spear PG (2007) Random linker-insertion mutagenesis to identify functional domains of herpes simplex virus type 1 glycoprotein B. *Proc Natl Acad Sci USA* 104(32): 13140–13145.
25. Gallagher JR, et al. (2014) Functional fluorescent protein insertions in herpes simplex virus gB report on gB conformation before and after execution of membrane fusion. *PLoS Pathog* 10(9):e1004373.
26. Park HE, Gruenke JA, White JM (2003) Leash in the groove mechanism of membrane fusion. *Nat Struct Biol* 10(12):1048–1053.
27. Roche S, Rey FA, Gaudin Y, Bressanelli S (2007) Structure of the prefusion form of the vesicular stomatitis virus glycoprotein G. *Science* 315(5813):843–848.
28. Kielian M, Rey FA (2006) Virus membrane-fusion proteins: more than one way to make a hairpin. *Nat Rev Microbiol* 4(1):67–76.
29. Zeev-Ben-Mordehai T, Vasishtan D, Siebert CA, Grünewald K (2014) The full-length cell-cell fusogen EFF-1 is monomeric and upright on the membrane. *Nat Commun* 5:3912.
30. Pertel PE, Fridberg A, Parish ML, Spear PG (2001) Cell fusion induced by herpes simplex virus glycoproteins gB, gD, and gH-gL requires a gD receptor but not necessarily heparan sulfate. *Virology* 279(1):313–324.
31. Mastronarde DN (2005) Automated electron microscope tomography using robust prediction of specimen movements. *J Struct Biol* 152(1):36–51.
32. Sandberg K, Mastronarde DN, Beylkin G (2003) A fast reconstruction algorithm for electron microscope tomography. *J Struct Biol* 144(1-2):61–72.
33. Nicastro D, et al. (2006) The molecular architecture of axonemes revealed by cryoelectron tomography. *Science* 313(5789):944–948.
34. Heymann JB, Belnap DM (2007) Bsoft: Image processing and molecular modeling for electron microscopy. *J Struct Biol* 157(1):3–18.
35. Eswar N, et al. (2006) Comparative protein structure modeling using Modeller. *Curr Protoc Bioinformatics* Chapter 5:Unit 5.6.
36. Pettersen EF, et al. (2004) UCSF Chimera–a visualization system for exploratory research and analysis. *J Comput Chem* 25(13):1605–1612.
37. Pintilie GD, Zhang J, Goddard TD, Chiu W, Gossard DC (2010) Quantitative analysis of cryo-EM density map segmentation by watershed and scale-space filtering, and fitting of structures by alignment to regions. *J Struct Biol* 170(3):427–438.
38. Garzón JI, Kovacs J, Abagyan R, Chacón P (2007) ADP_EM: Fast exhaustive multiresolution docking for high-throughput coverage. *Bioinformatics* 23(4):427–433.
39. Kawabata T (2008) Multiple subunit fitting into a low-resolution density map of a macromolecular complex using a gaussian mixture model. *Biophys J* 95(10):4643–4658.
40. Lasker K, Topf M, Sali A, Wolfson HJ (2009) Inferential optimization for simultaneous fitting of multiple components into a CryoEM map of their assembly. *J Mol Biol* 388(1):180–194.
41. Pandurangan AP, Shakeel S, Butcher SJ, Topf M (2014) Combined approaches to flexible fitting and assessment in virus capsids undergoing conformational change. *J Struct Biol* 185(3):427–439.
42. Vasishtan D, Topf M (2011) Scoring functions for cryoEM density fitting. *J Struct Biol* 174(2):333–343.
43. Topf M, et al. (2008) Protein structure fitting and refinement guided by cryo-EM density. *Structure* 16(2):295–307.
44. Mackeen MM, et al. (2010) Small-molecule-based inhibition of histone demethylation in cells assessed by quantitative mass spectrometry. *J Proteome Res* 9(8):4082–4092.
45. Ishihama Y, et al. (2005) Exponentially modified protein abundance index (emPAI) for estimation of absolute protein amount in proteomics by the number of sequenced peptides per protein. *Mol Cell Proteomics* 4(9):1265–1272.
46. Trudgian DC, et al. (2011) Comparative evaluation of label-free SINQ normalized spectral index quantitation in the central proteomics facilities pipeline. *Proteomics* 11(14):2790–2797.

Supporting Information

Zeev-Ben-Mordehai et al. 10.1073/pnas.1523234113

SI Materials and Methods

Immunogold Labeling. Plasma-cleaned, formvar carbon film-coated, 300 mesh, copper grids (Electron Microscopy Sciences) were incubated 2 min on 5-μL drops containing gB vesicles. Dilutions were optimized for each vesicle preparation. After two washing steps on 50-μL drops of wash buffer (0.1% BSA in PBS), grids were incubated on 50-μL drops containing buffer A (1% BSA in PBS) or R218 anti-gB polyclonal Ab (a gift from Gary H. Cohen and Roselyn Eisenberg, University of Pennsylvania, Philadelphia) (8 μg/mL in buffer A) in a wet chamber for 3 h at room temperature. After five washes on wash buffer, grids were incubated for 30 min on 20-μL drops of 1:40 dilutions of anti-rabbit IgG-gold conjugate (5-nm particle size) in wash buffer. Before negative staining, grids were washed on five drops of wash buffer, followed by five washes on water drops. Staining was done on 2% NanoW (Nanoprobes) drops for 10 s before drying.

Negative Stain Imaging. Imaging was performed using a TF30 electron microscope (FEI) operated at 200 keV. Images were recorded on a US4000 CCD ~4,000 × 4,000 camera (Gatan) with a calibrated pixel size of 0.295 nm at specimen level and a defocus of −5.5 μm using SerialEM (31). After recording of overview images in lower magnification on various regions of the grid, random spots containing vesicles were marked and imaged at the indicated magnification.

Subvolume Averaging. For the reconstruction of the short form of gB (Fig. S2), particle subvolumes were picked manually from two sets of tomograms. Each was from independent (i.e., different cell culture) preparation of gB vesicles, comprising eight tomograms with 881 particles and four tomograms with 1,381 particles, respectively. Both sets of tomograms were binned fourfold, and the particles were aligned separately to confirm that each dataset converged to similar structures. The averages from both datasets showed strong threefold symmetry. For removal of duplicate particles, groups of particles with center-to-center distances of <80 Å were removed, except for the one representative with the highest cross-correlation value to the reference. The remaining particles were merged into one dataset of 1,909 particles. Tilt orientations (axes normal to the membrane) and positions were kept from the previous alignments, but the twist angle (angle around symmetry axis) for each particle was randomized. Ten iterations of twist alignment were performed on fourfold binned particles, and six iterations of further refinement were then performed around all axes on twofold binned particles. This structure showed the same strong threefold symmetry as seen before. Thus, two extra particles were added for each particle already picked, each with the same tilt angle and position as the original but with either 120° or 240° of twist rotation applied. A further three iterations of refinement were run. The resulting map was resymmetrized (C3) and filtered to the resolution given by the FSC (Fig. S4; details are provided below). All alignments were done using PEET 1.9 (33).

Gold-standard FSC calculation was performed by splitting the merged 1,909-particle dataset into odd and even particles, and applying the same refinement procedure to both independently. The split averages were aligned and masked using a custom mask based on segmentation of the merged average. To avoid correlation between the masks, one average was masked with a hard-edged mask and the other with a soft-edged one. The FSC, calculated using Bsoft (34), is 27 Å at the 0.5 criterion and 23 Å at the 0.143 criterion.

For the reconstruction of the long form of gB (Fig. S3), 457 particles were picked manually from a total of nine tomograms. All tomograms were fourfold binned. Five iterations of tilt and shift alignment were applied to the entire dataset. Duplicate particles were removed as before, leaving 395 particles. Five iterations of twist refinement were then applied on twofold binned particles, followed by five iterations of minor refinement around every axis. C3 symmetry was applied as in the short-form refinement, and a further four iterations of refinement were applied. The resulting map was resymmetrized (C3) and filtered to the resolution given by the FSC.

The FSC calculation was made by splitting the 395-particle dataset into two halves and refining them separately. The two halves were aligned and masked with a short cylindrical mask that contains only the protein, one soft-edged and one sharp-edged. The FSC was 36 Å at the 0.5 criterion and 31 Å at the 0.143 criterion.

Model Building. A model combining Protein Data Bank ID codes 2GUM and 3NWF was built using MODELER (35). It contains the coordinates of the FLs at neutral pH (resolved in 2GUM, residues 261 and 262) with the additional regions resolved at acidic pH (present in 3NWF, residues 331–337 and 460–476).

The density corresponding to the membrane bilayer was first removed using the *crop* tool in Chimera (36). The resulting density map was segmented using the Segger tool (37) with default values. The segmented densities were visually inspected and manually grouped to include only segments from the gB trimer.

For the fitting of domain I (residues 154–363), four independent ensembles of fits were generated using different rigid fitting methods that vary on the space-sampling method and/or criteria used to assess the quality of fit of the resulting models. Ensemble 1 was created using the *Fit_in_map* global search function in Chimera (36), sampling 1,000 initial random points within the density map. Ensemble 2 was generated with ADP_EM (38) setting a bandwidth of 32 and using translational sampling of 4.6 Å (single-voxel size), a density threshold of 1.63, and the exhaustive search mode. GMFit (39) was used to generate Ensemble 3 by fitting three copies of domain I into the density map. The number of Gaussians for each individual domain and the density map was set to eight and 15, respectively. The number of initial configurations, the number of configurations for the local search, and the number of output configurations were set to 1,000, 100, and 50 respectively. Ensemble 4 consisting of 50 fits was generated using the MultiFit tool (40) implemented in Chimera. The density threshold, the resolution of the map and the sampling rate were set to 1.63, 22 Å, and 15°, respectively. The latter two ensembles were generated using the threefold rotational symmetry option available for the respective program. For the first two ensembles, two threefold symmetrical copies were added to the final results using the *sym* command in Chimera. From each method, the 30 top-ranking models were collected, resulting in a new ensemble of 120 models in total.

Next, two complementary scores were computed for each domain I fit, the segment-based cross-correlation coefficient (SCCC) (41) and an atom protrusion score (APS), we have implemented in TEMPy (42). The APS calculates the fraction of atoms in a given model/protein that protrude out of the envelope of the EM density map as follows:

$$APS = \frac{n}{N}, \quad \textbf{[S1]}$$

where N is the total number of backbone atoms and n is the number of backbone atoms protruding outside the envelope.

The envelope is defined by a set of voxels for which the density values are above a given threshold ε:

$$n = \sum_{bb=1}^{N} \delta(x) \begin{cases} 1, voxel_{density_{bb}} < \varepsilon \\ 1, voxel_{density_{bb}} \geq \varepsilon \end{cases}, \quad \textbf{[S2]}$$

where $voxel\_density_{bb}$ is the density value of the voxel occupied by the backbone atom bb and ε is the threshold value. Here, the value of ε was set to 1.63 (1 SD from the mean of the density map).

A combined score integrating both measures was used for calculating the goodness of fit by taking the difference between SCCC and APS scores (ranging between −2 and 1). Using this score, the 120 domain I fits were then clustered by a hierarchical clustering method based on both the score and the Cα-rmsd between the fits. The cluster cutoffs between 7 Å and 17 Å were tested, and the value of 13 Å was selected based on the number of clusters and cluster size distribution (Fig. S6), resulting in 50 clusters. Within each cluster, the top-scoring fit was chosen as a representative. The 10 top-scoring representatives were selected for further assessment. These fits were filtered based on backbone clashes between protomeric units using Chimera, resulting in seven fits positioning domain I in the membrane-distal region of the map. Next, the postfusion crystal structure of both domains I and II (residues 142–153 and 354–460) was superimposed on each fit of domain I. Using the superimposed domain II as the starting position, an ensemble of 250 configurations of domain II was generated (allowing a ±60° rotation and 3-Å translation) and symmetrized (threefold) using TEMPy (42) in the context of the map. The resulting 1,750 domain II fits were scored (as before) and filtered using backbone clashes and distance constraints between domain I and domain II. Distance constraints were based on the maximum length possible for the linker regions between residues 152–157 and 355–366, respectively. The scores of the remaining models clearly discarded all domain I models oriented with the FLs pointing toward the membrane (Fig. 3). To complete the fit, we ran four iterations of Flex-EM (43) on the top four models to refine the position of domain II in the map further and confirm that the linkers were capable of joining the two domains without breaking bond restraints.

For domain IV (residues 111–116 and 573–660) positioning, an ensemble of 210 fits was generated with Chimera as described earlier, and the threefold symmetrized fits were scored (as above), clustered, and filtered using backbone clashes between the domain IV fits and the previously obtained domain I and II models. After testing (Fig. S7), a Cα-rmsd cutoff of 9 Å was chosen for clustering, yielding 151 clusters. Only 50 fits passed this filtering step. The four best-scoring fits were selected (the score distribution showed a drastic drop after model 4). Although the selected fits did not converge to a single orientation of domain IV, they were all located in the midlevel density, neighboring domain II (Fig. S7).

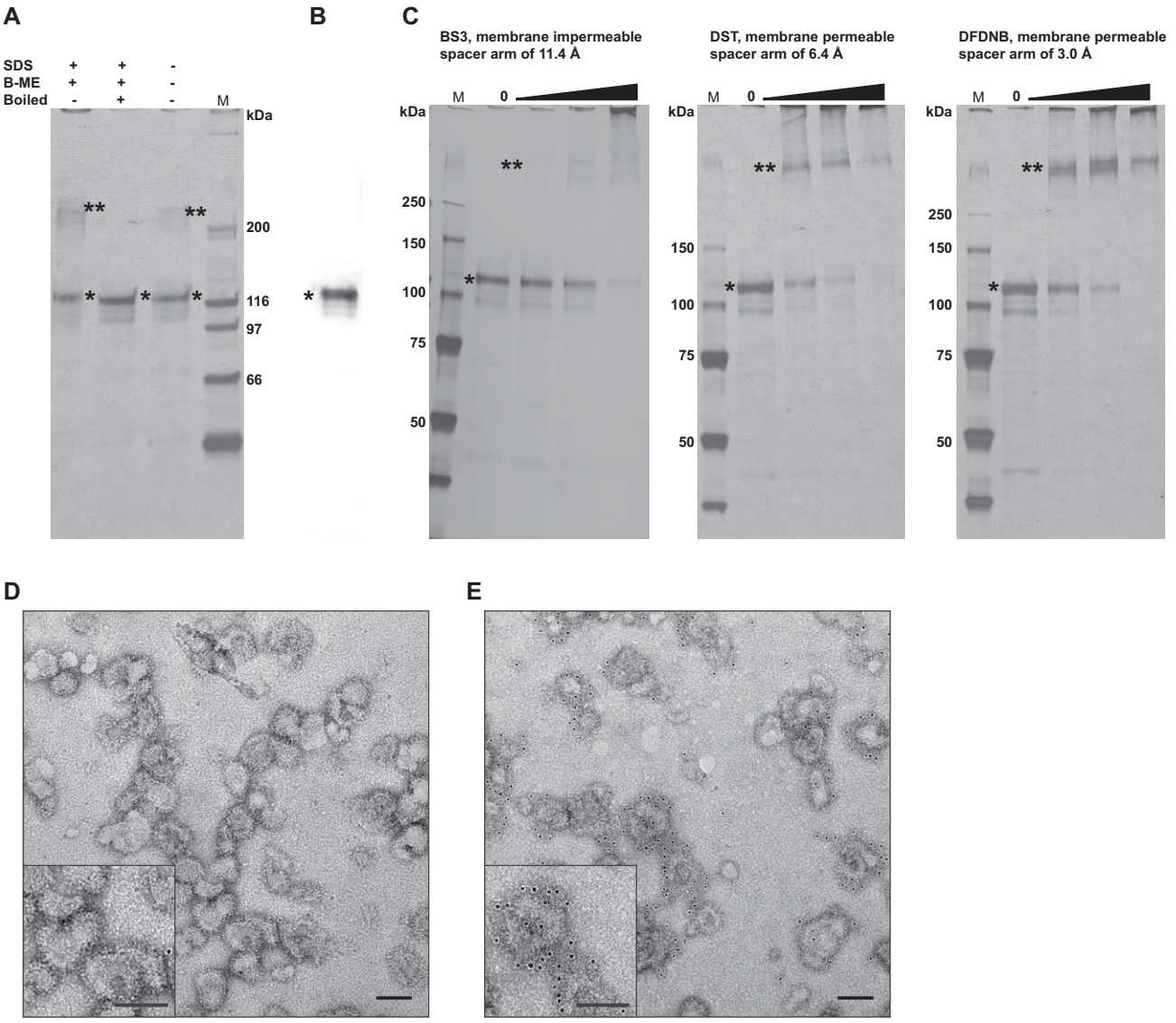

Fig. S1. Analysis of gB vesicles. (*A*) SDS/PAGE analysis under denaturing and "seminative" conditions. A single asterisk marks the monomer, and two asterisks mark oligomers. (*B*) Denaturing Western blot using polyclonal Ab R218. (*C*) Chemical cross-linking of full-length gB on vesicles using bis[sulfosuccinimidyl] suberate (BS3), disuccinimidyl tartrate (DST), and DFDNB. Products of the cross-linking reaction using 0–5 mM cross-linker were run on a 4–15% precast SDS/PAGE gel, along with high-molecular-mass markers and precision plus standards (Bio-Rad). Gels were silver-stained. A single asterisk marks the monomer, and two asterisks mark trimers. (*D* and *E*) Immunogold labeling of gB vesicles. No primary Ab (*D*) or the polyclonal anti-gB Ab R218 (*E*) followed by anti-rabbit IgG-gold (5 nm; Aurion) conjugate labeling was used. Dark black particles with white fringe are the gold beads. (Scale bars, 100 nm.)

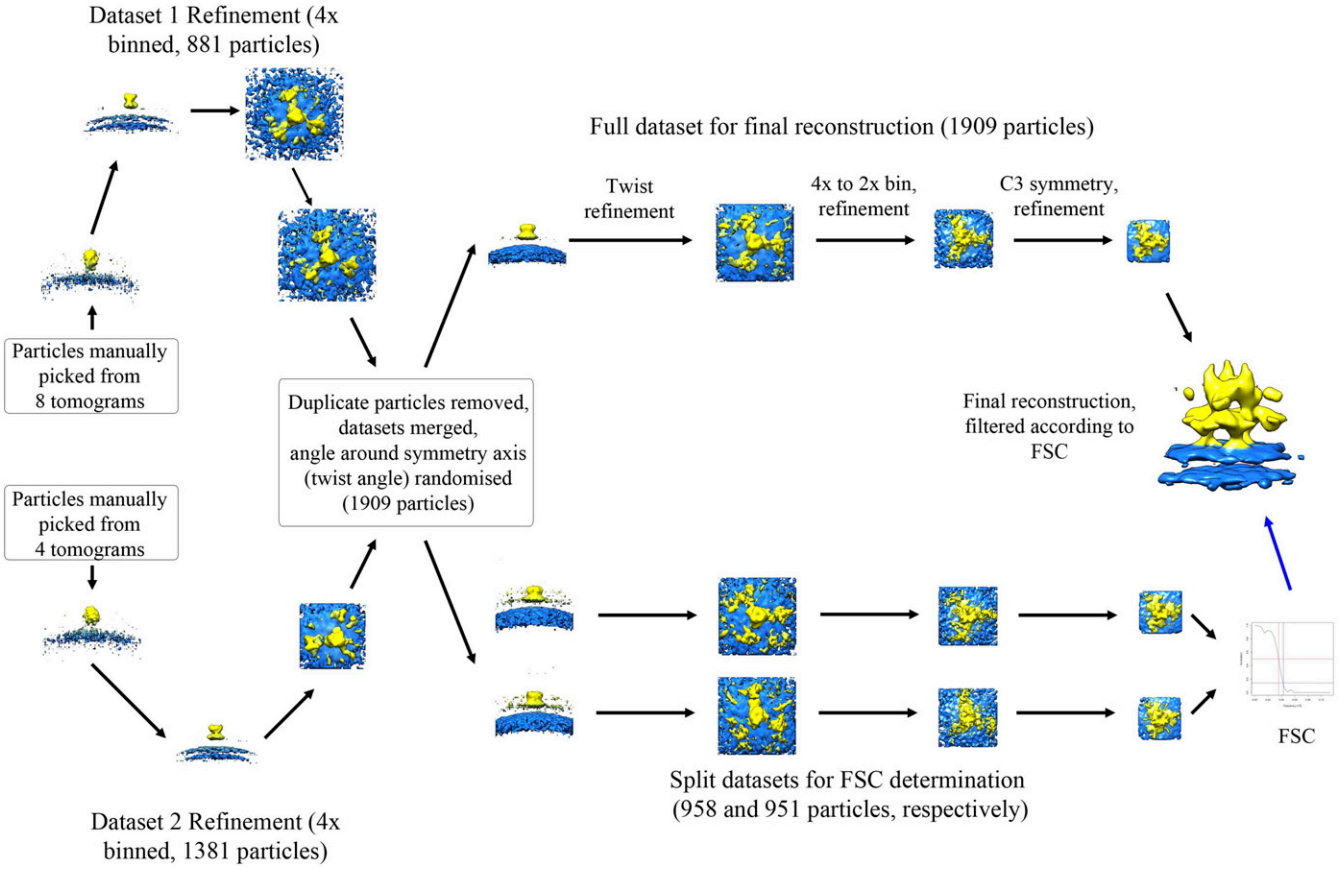

Fig. S2. Depiction of the subvolume averaging workflow for the reconstruction and FSC determination of the short-form gB structure. Two biologically independent datasets, with 881 and 1,381 particles, were separately refined before being cleaned of duplicate particles and merged for the final reconstruction and FSC determination (results and curves are shown in Fig. S4). Displayed density maps (protein colored yellow and membrane colored blue) are actual intermediate structures created at the end of each step. Top views are presented when the symmetry was apparent. The overall size of each structure is determined by the box size, and does not reflect any changes in binning. Twofold binned structures are Gaussian-filtered for visualization purposes.

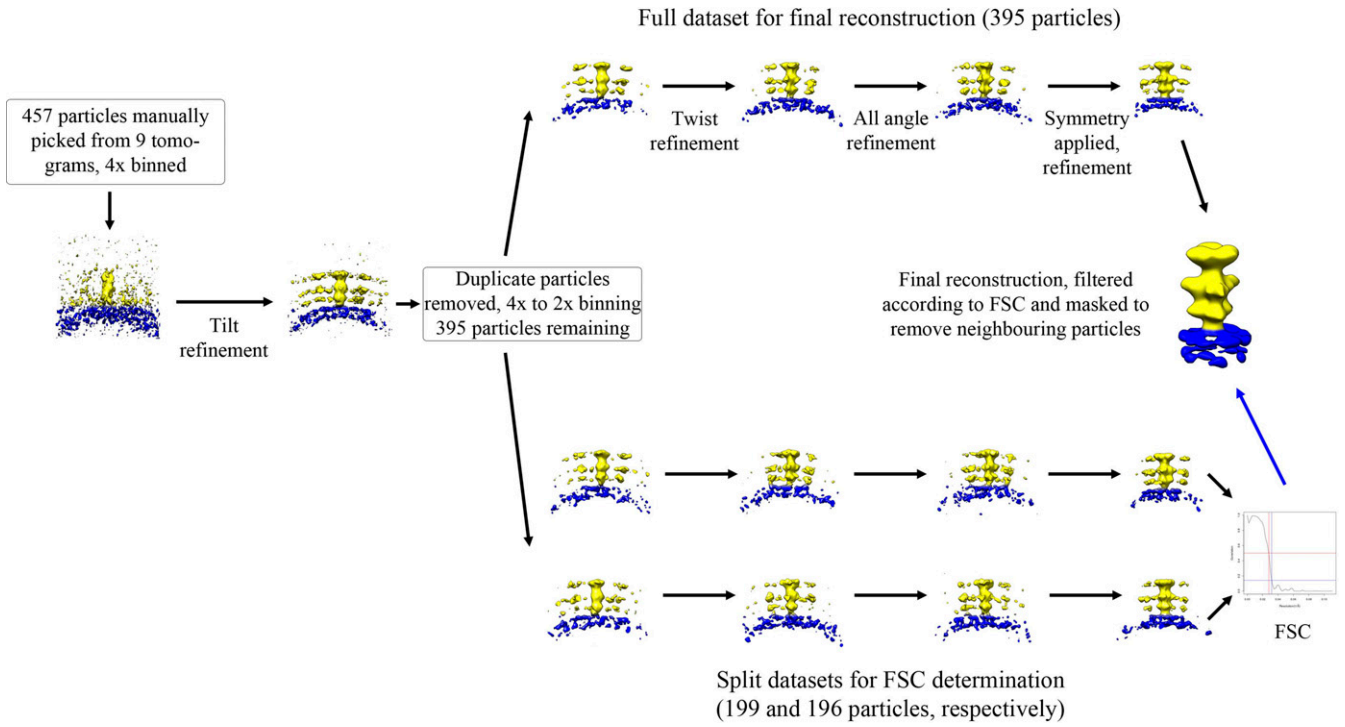

Fig. S3. Depiction of the subvolume averaging workflow for the reconstruction and FSC determination of the long-form gB structure. Four hundred fifty-seven particles were refined in tilt angle and position before being cleaned of duplicate particles for the final reconstruction and FSC determination (results and curves are shown in Fig. S4). The density maps shown (protein colored yellow and membrane colored blue) are actual intermediate structures created at the end of each step. The overall size of each structure is determined by the box size, and does not reflect any changes in binning. Twofold binned structures are Gaussian-filtered for visualization purposes. To remove obscuring neighboring densities, all densities are clipped to show the central planes.

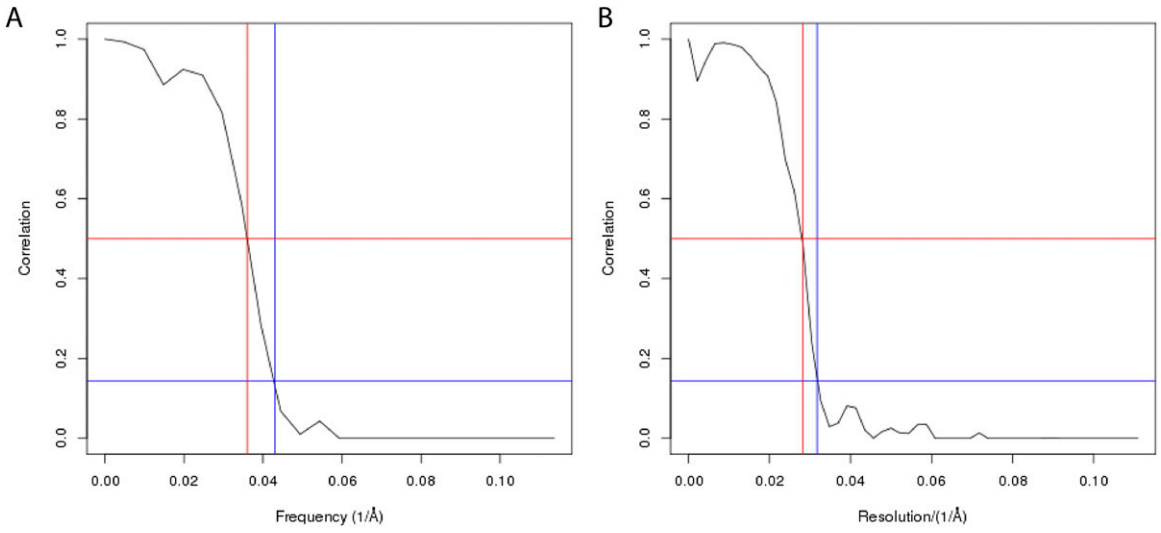

Fig. S4. FSC curves for the gold-standard resolution (compare Figs. S2 and S3) determined for the short (*A*) and long (*B*) forms.

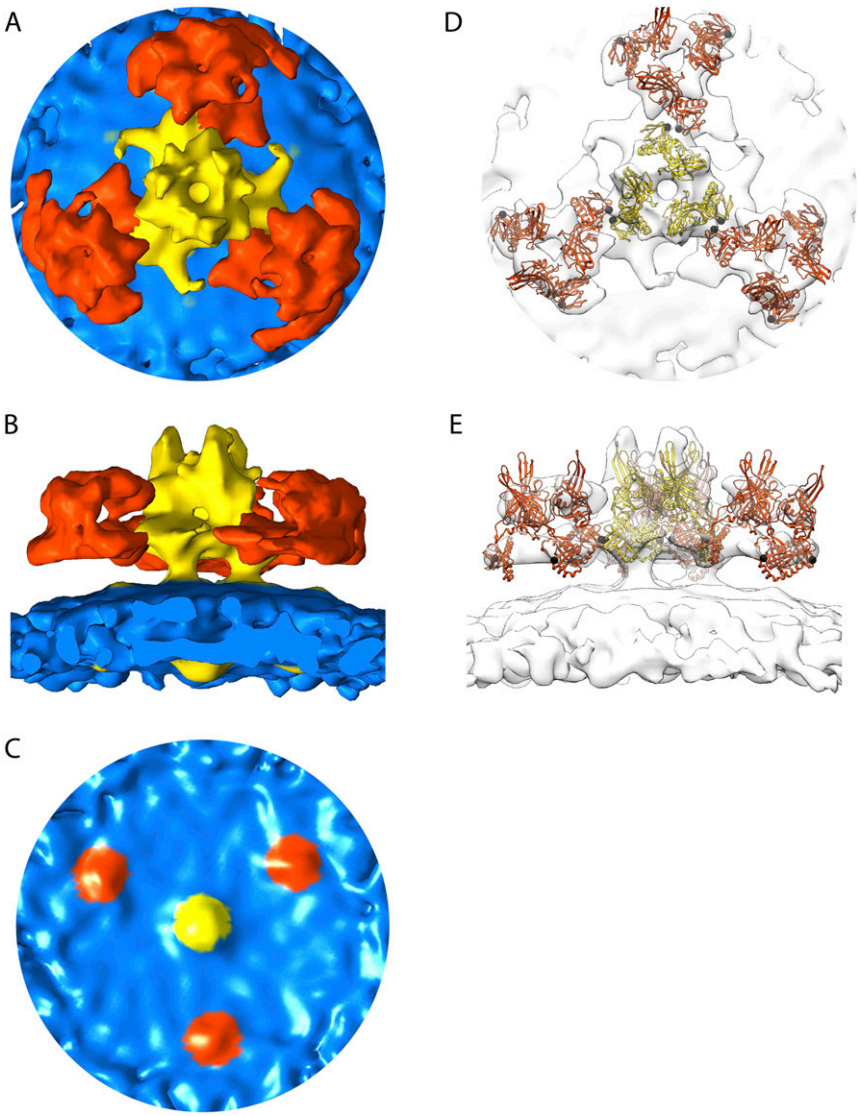

Fig. S5. CryoET map of the short form shown at a higher threshold to highlight neighboring protein particles. (*A*–*C*) Top, side, and bottom views. The main density is colored yellow, and neighbors are colored orange. (*D* and *E*) Fitting of the prefusion structure into the neighbor density maps. Glycosylation site N398 (black sphere) is facing neighboring gB trimers.

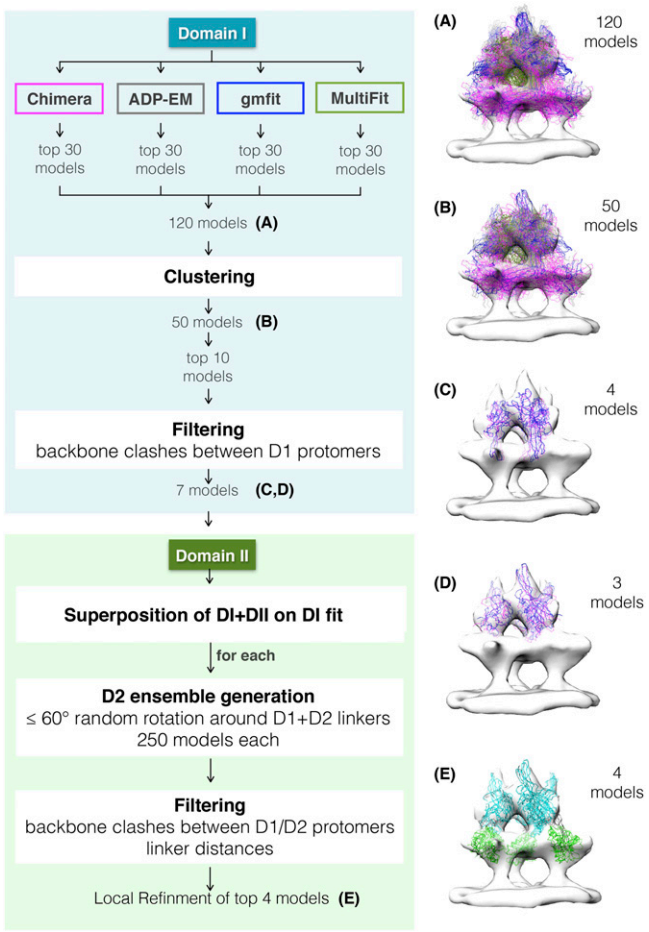

Fig. S6. Workflow for model building. (*Left*) Diagram summarizing the procedure used to derive the position of domains I and II in the density map. Using the crystal structure of domain I from the postfusion conformation [Protein Data Bank (PDB) ID code 2GUM], the 30 top-scoring fits generated by four different fitting methods were collected. The corresponding threefold symmetrical models were scored and subjected to clustering and filtering based on backbone clashes between protomeric units, resulting in seven domain I fits (more details are provided in *Materials and Methods*). (*Right*) Sampled space for domain I at each step of the process. Trimeric domain I fits are shown in Cα-trace representation and color-coded according to the method from which they derive [i.e., magenta, *Chimera Fit in map* function (36); gray, ADP_EM (38); blue, GMFit (39); olive, MultiFit (40)]. (*A*) Ensemble of 120 domain I fits collected from the four fitting methods. (*B*) Fifty cluster representatives remaining after this step. (*C* and *D*) Seven domain I fits remaining after the filtering step. All of them position domain I in the membrane-distal density of the map, indicating two overall different possible orientations: with the FLs pointing toward (*C*) or away (*D*) from the membrane. This subset of seven fits was further assessed using structural constraints to domain II. For each of the seven domain I fits obtained at this stage, the crystal structure of domains I + II from the postfusion conformation was superimposed to the domain I fit and an ensemble of 250 domain II fits was generated therein. The resulting domain II fits (1,750 in total) were filtered based on backbone clashes and distance constraints between domain I and II protomeric units. The four top-scoring fits were subjected to further local refinement. (*Right*) Map sampled by domain I and II fits. (*E*) Locally refined domain II fits resulting from the described fitting procedure. Fits are shown in Cα-trace representation with domain I colored cyan and domain II colored green.

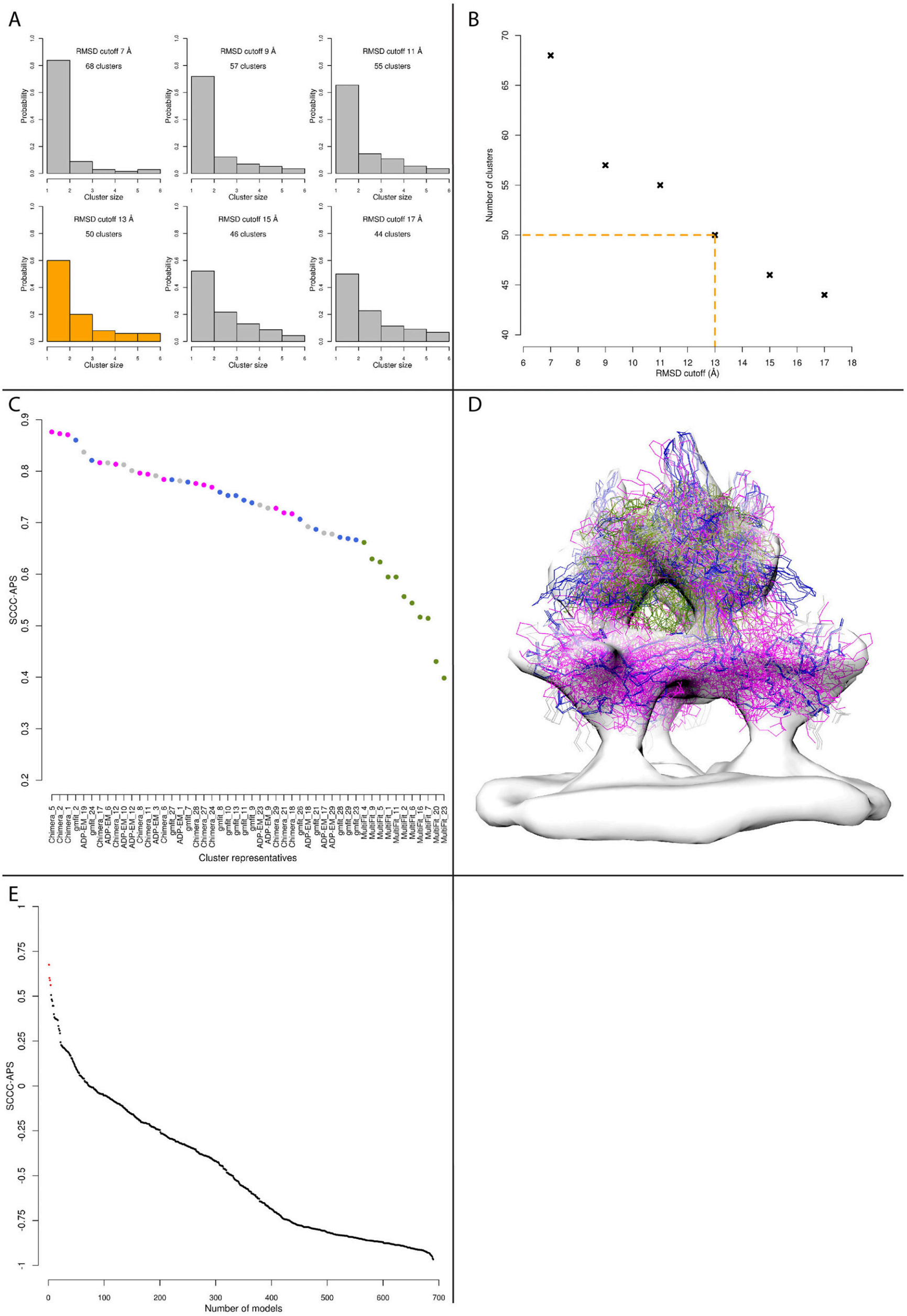

Fig. S7. Clustering and scoring results. (*A–D*) Clustering of the 120 domain I fits. (*A*) Cluster size histograms for each Cα-rmsd cutoff tested. The histogram corresponding to the chosen Cα-rmsd cutoff (13 Å) is indicated in orange. (*B*) Number of clusters vs. tested Cα-rmsd cutoff. Dashed lines highlight the number of clusters for the chosen Cα-rmsd cutoff (13 Å). (*C*) SCCC-APS scores of cluster representatives. Models are ranked in descending order of scores and color-coded according to the fitting method from which each model was derived. (*D*) Space sampled by the cluster representatives ($n = 50$) resulting from the chosen Cα-rmsd. Cluster representatives are shown as Cα-traces for clarity and color-coded as in *C*. (*E*) SCCC-APS scores of cluster representatives for domain II.

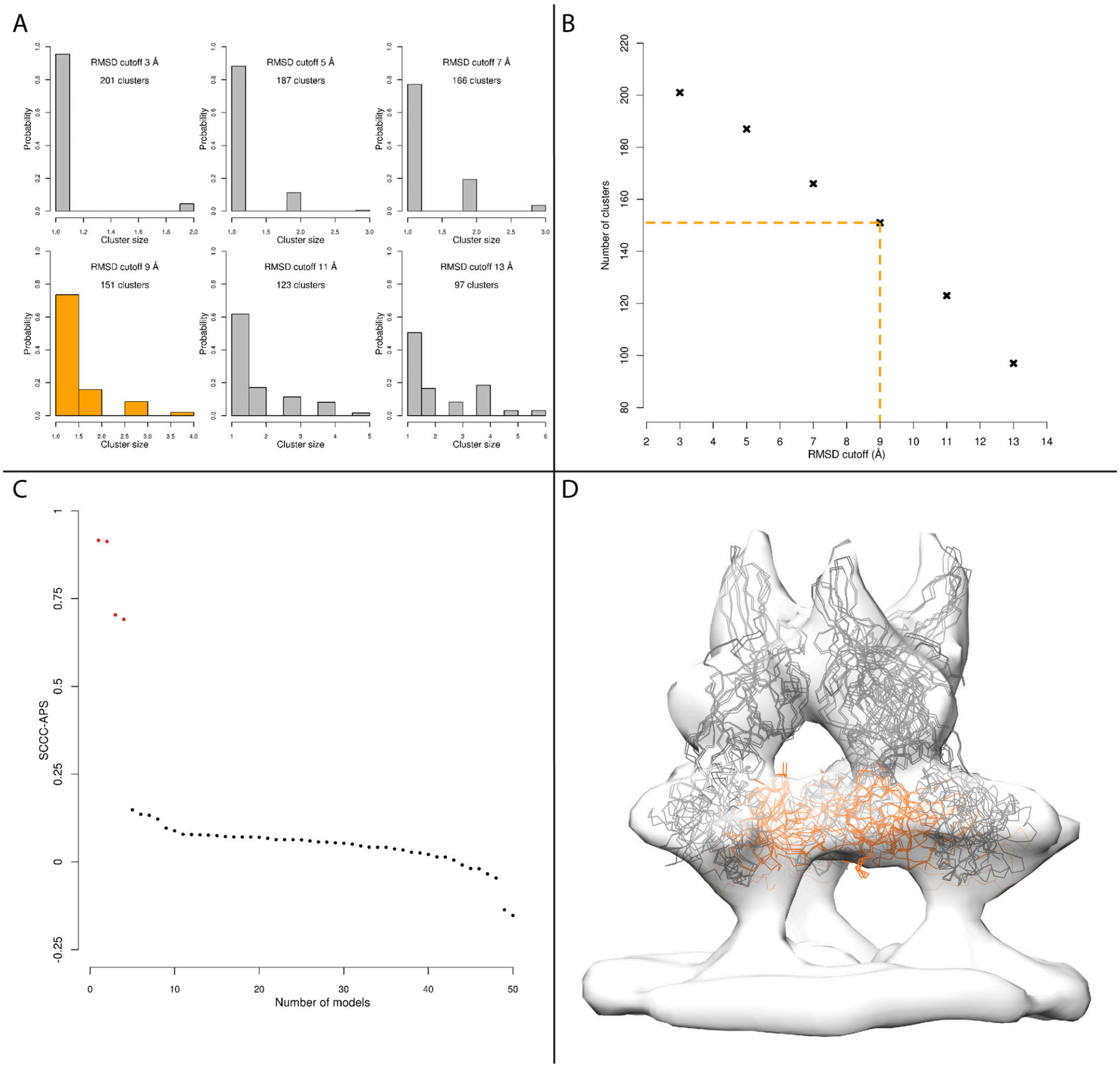

Fig. S8. Domain IV fitting. Clustering of domain IV fits. (*A*) Cluster size histograms for each Cα-rmsd cutoff tested. The histogram corresponding to the chosen Cα-rmsd cutoff (9 Å) is indicated in orange. (*B*) Number of clusters vs. tested Cα-rmsd cutoff. Dashed lines highlight the number of clusters for the chosen Cα-rmsd cutoff (9 Å). (*C*) SCCC-APS scores of cluster representatives that pass backbone clashes filtering. Models are ranked in descending order of scores. (*D*) Domain IV fits resulting from the described procedure.

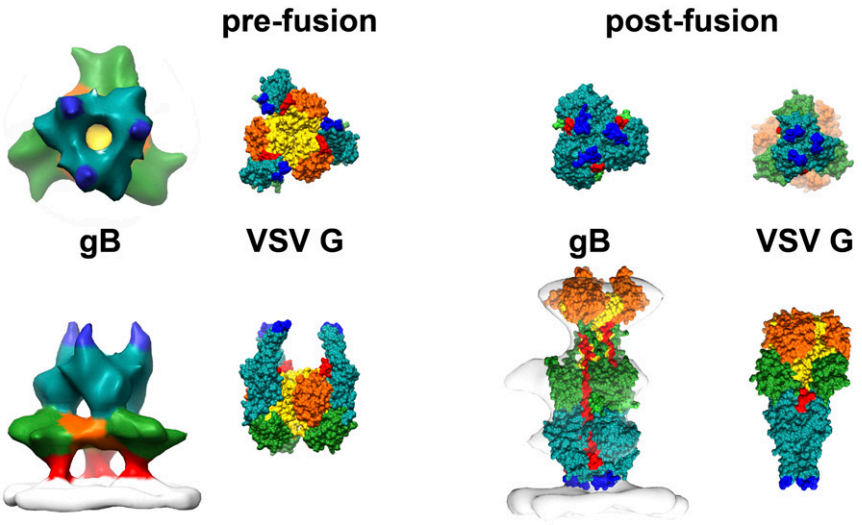

Fig. S9. Comparison between the two conformations of HSV-1 gB and VSV G pre- and postfusion conformations. Surface representations of the crystal structures of the VSV G prefusion (PDB ID code 2J6J) and postfusion conformation (PDB ID code 2CMZ) are shown in comparison to the two forms of gB in the membrane. The postfusion gB crystal structure (PDB ID code 2GUM) is fitted in the respective EM map. Domain coloring is as in Fig. 4. The upper row shows the view from the FL face, and the lower row shows the side view.

Table S1. Major proteins identified by MS in the vesicle preparations and their relative abundance

				HSV-1 gB		
Protein name	Subcellular location*	UniProt accession no.	Mass, Da	Score[†]	emPAI[‡]	Relative abundance,[§] %
Envelope gB HSV-1	Virion membrane	P06437	100,875	4,375	36.84	18
Peptidyl-prolyl *cis-trans* isomerase A	Cytoplasm	P14851	18,059	289	28.3	13
Tubulin beta	Cytoplasm	Q2KJD0	50,095	558	28.26	13
Histone H4	Nucleus	Q4R362	11,360	235	23.85	11
14-3-3 protein epsilon	Cytoplasm	P62258	29,326	259	22.72	11
Actin	Cytoplasm	A2BDB0	42,108	971	17.89	9
Vimentin	Cytoplasm	P02544	53,754	815	17.2	8
EH domain-containing protein 4	Cytoplasm	Q9EQP2	61,670	599	14.36	7
Pyruvate kinase	Cytoplasm	P52480	58,378	816	11.22	5
Moesin	Cytoplasm	P26041	67,839	664	10.95	5

*Based on UniProt annotation.
[†]Mascot score for confidence of protein identification is defined as the −log value of the probability *P* that this assignment is made by chance (44).
[‡]emPAI analysis (45, 46).
[§]Relative abundance with respect to the proteins with the highest emPAI listed in this table.

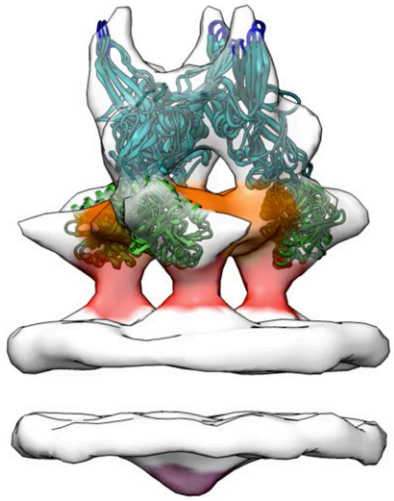

Movie S1. Complementary movie to Fig. 3, showing the prefusion structure of gB.

Movie S1

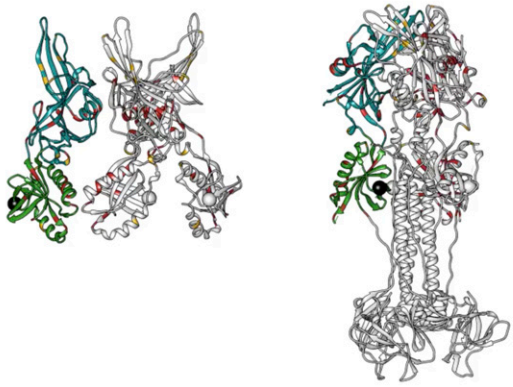

Movie S2. Complementary movie to Fig. 4, highlighting the positions of 5-aa and fluorescence protein insertions on the pre- and postfusion structures of gB.

Movie S2